Journal Article

Thin film flow on a vertically rotating disc of finite thickness partially immersed in a highly viscous liquid

Miah, M.S., Al-Assaf, S., Yang, X. and McMillan, A.

Thin film flow on a vertically rotating disc of finite thickness partially immersed in a highly viscous liquid

Md Salim Miah*[a,b], Saphwan Al-Assaf[a], Xiaogang Yang[a], Alison McMillan[a]

[a]Applied Sciences, Computing and Engineering Division
Glyndŵr University, Wrexham, LL11 2AW, UK
[b]Present address and address for correspondence: Aeronautical Engineering Department,
Military Technological College, P.O Box 262, P.C 111, Sultanate of Oman

*Corresponding Author's E-mail Address: MD.Salim@mtc.edu.om

HIGHLIGHTS

- The film formation is investigated experimentally and modelled numerically.
- A correlation equation has been proposed to predict the film thickness.
- The experimental measurements were conducted using the laser scan method.
- Numerical modelling was performed using the Volume of Fluid method.
- The rim thickness of the disc was found to have a measurable effect on the film profile.

ABSTRACT

The entrainment and flow of a thin film of liquid on a vertically rotating disc partially immersed in a liquid bath has been investigated experimentally and modelled numerically. The Volume of Fluid (VOF) Computational Fluid Dynamics (CFD) modelling approach has been employed to characterise the shape and stability of the thin film thickness profile. The thickness of the rotating disc plays a significant role in the thin film profile and this is confirmed through the comparison of simulation with the experimental results. Other factors determining the film thickness were identified as the rotational speed and the fluid viscosity where the film thickness profile increases with the increase of the rotational speed and also the viscosity. A correlation equation to predict the film thickness as a function of angular position, radius, rotating speed, viscosity and surface

tension is proposed. The results given in this study specifically report on the thin film thickness variation with the angular direction and the film entrained into the liquid. In both the simulation and experimental results, it is noted that the film thickness stabilises following a rotation of 15° after drag out of the liquid, and remains so until 10° before being dragged back in.

Keywords:

Thin film
Rotating disc
Volume of Fluid
Computational Fluid Dynamics (CFD)
Mathematical model
Laser scan

1. Introduction

Thin film flows on vertical rotating discs are extensively used in the extrusion coating process, in which a polymeric material is extruded on to another polymeric material to form a composite laminate [1]. Other typical examples include that of the oil disc skimmers, which are used for oil recovery as an alternative to toxic chemical dispersants in case of an offshore oil spill. In the synthesis of polyethylene terephthalate (PET) in polycondensation reactors [2], a series of vertically rotating discs are partially immersed in highly viscous polymer liquid, where the melt is picked up and spread, in the form of a thin film, onto the surface of the discs. This achieves an enhanced mass transfer from melt to film, enabling the low-cost production of plastic bottles and food packaging boxes.

While there have been many studies of thin film flows on horizontally rotating discs [3, 4], there have been limited studies [5, 6] on the vertical case. Unlike the horizontal case, the film flow in a vertically rotating system is always associated with a meniscus region, where the liquid is dragged out of the tank by the rotation of the disc. As a result, an unstable oscillating region is set up, where the film formed on the disc is dragged back into the liquid tank. The fluid dynamical aspects are

still not fully investigated, although there are some discussions and general solutions of film thickness profiles for the problem of liquid drag out [7, 8].

In the present study there are two aims: to formulate a relationship for thickness as a function of position on the disc, and to examine the effect of disc rim thickness on the film formation process. It is important to recognise that as a result of the film formation process, the film thickness distribution in different radial and angular positions on the disc surface is not uniform [9]. The simulation results of this study confirm that the flow entrained onto the rim of the disc has a non-negligible effect on the film formation on the disc surface leading to a change in the film thickness profile relative to that of an idealised "thin" disc. Results for two disc rim thickness are presented here.

The computational model for the liquid thin film flow consists of expansive tank of liquid, partially bounded by a solid substrate with a free surface (the rotating disc), where the liquid is exposed to another fluid, usually a gas and most often air in applications [10]. To describe the physical phenomena of the liquid film flow, the Navier-Stokes equation is used, which presented here in cylindrical coordinate form [9, 11, 12]. The mathematical model proposed by Afanasiev *et.al.* [9] is extended to define the film pattern formation. The mathematical model must be solved numerically, but simplifications can be applied on the basis of non-dimensional analysis. In this study the CFD code employed is ANSYS Fluent 6.3 [13], and the Volume of Fluid (VOF) method is employed for tracking and locating the free surface.

In the modelling of the film formation, it is important to consider the force balance, as the shape and stability of the thin film is controlled by the forces acting on it: viscous, inertial, surface tension, centrifugal, coriolis and gravitational forces. For a vertically rotating disc with low rotational speeds in the order of 1 rpm to 6 rpm, the Coriolis force can be neglected at the leading order, as the Coriolis force term is of the same order as the inertial force terms, following lubrication theory [14, 15].

The numerical simulations data have been validated through a comprehensive experimental investigation. The experiments were conducted in a laboratory scale experimental device as described in the experimental section and the measurements were performed using the laser scan

method [16]. The experimental and numerical simulation results obtained illustrate a good agreement.

NOMENCLATURE

Ca	[-]	Capillary number
d	[m]	Immersion depth
d'	[-]	Dimensionless immersion depth
Fr	[-]	Froude number
g	[m/s^2]	Gravitational acceleration
h	[m]	Thin film thickness
h'	[-]	Dimensionless film thickness
R	[m]	Disc radius
k	[-]	Curvature of the free surface
R'	[-]	Dimensionless disc radius
Re	[-]	Reynolds number
T	[s]	Time
t'	[m]	Thickness of rotating disc
We	[-]	Webber number

Special characters

α	[-]	Aspect ratio of the flow
θ	[^{0}]	Angular coordinate
Ω	[rpm]	Rotating speed
ν	[m^2/s]	Kinematic viscosity
ρ	[kg/m^3]	Density
μ	[Pa.s]	Dynamic viscosity
σ	[N/m]	Surface tension
ω	[rad/s]	Angular velocity

Subscripts

CFD	Computational fluid dynamics
CFL	Courant-Friedrich-Lewy condition
VOF	Volume of fluid
PET	Polyethylene terephthalate

2. Mathematical modelling

The physical set up for the vertically rotating disc partially immersed in liquid is shown in Figure 1. A disc of radius R is rotating at angular velocity Ω about its horizontal axis, which is a distance d above the liquid bath. For most thin film flows on vertically rotating discs, the flows can be treated as incompressible [9].

For the problem of the vertically rotating disc, the cylindrical coordinate system is employed for convenience. Let the liquid velocity vector to be represented by (u_r, u_θ, u_z) and ω denote the angular velocity vector with components $(0,0,\Omega)$.

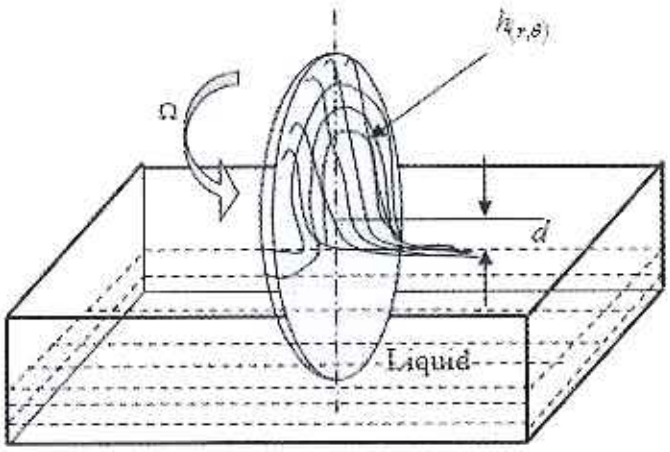

Figure 1. Configuration of a rotating disc partially immersed in liquid

2.1. Governing equations

The Navier-Stokes equations used to describe the thin film flow on a vertically rotational disc can be expressed in cylindrical coordinates as [9]:

$$\frac{\partial u_r}{\partial t}+u_r\frac{\partial u_r}{\partial r}+\frac{u_\theta}{r}\frac{\partial u_r}{\partial \theta}-\frac{u_\theta^2}{r}+u_z\frac{\partial u_r}{\partial z}=-\frac{1}{\rho}\frac{\partial p}{\partial r}+$$
$$\nu\left[\frac{\partial^2 u_r}{\partial r^2}+\frac{1}{r}\frac{\partial u_r}{\partial r}+\frac{1}{r^2}\frac{\partial^2 u_r}{\partial \theta^2}+\frac{\partial^2 u_r}{\partial z^2}-\frac{2}{r^2}\frac{\partial u_\theta}{\partial \theta}-\frac{u_r}{r^2}\right]-g\sin\theta \tag{1a}$$

$$\frac{\partial u_\theta}{\partial t}+u_r\frac{\partial u_\theta}{\partial r}+\frac{u_\theta}{r}\frac{\partial u_\theta}{\partial \theta}+\frac{u_r u_\theta}{r}+u_z\frac{\partial u_\theta}{\partial z}=-\frac{1}{\rho r}\frac{\partial p}{\partial \theta}+$$
$$\nu\left[\frac{\partial^2 u_\theta}{\partial r^2}+\frac{1}{r}\frac{\partial u_\theta}{\partial r}+\frac{1}{r^2}\frac{\partial^2 u_\theta}{\partial \theta^2}+\frac{\partial^2 u_\theta}{\partial z^2}+\frac{2}{r^2}\frac{\partial u_\theta}{\partial \theta}-\frac{u_r}{r^2}\right]-g\cos\theta \tag{1b}$$

$$\frac{\partial u_z}{\partial t}+u_r\frac{\partial u_z}{\partial r}+\frac{u_\theta}{r}\frac{\partial u_z}{\partial \theta}+u_z\frac{\partial u_z}{\partial z}=-\frac{1}{\rho}\frac{\partial p}{\partial z}+$$
$$\nu\left[\frac{\partial^2 u_z}{\partial r^2}+\frac{1}{r}\frac{\partial u_z}{\partial r}+\frac{1}{r^2}\frac{\partial^2 u_z}{\partial \theta^2}+\frac{\partial^2 u_z}{\partial z^2}\right] \tag{1c}$$

where ρ, μ, ν and p denote, respectively, the density, dynamic viscosity, kinematic viscosity and the pressure of the liquid. The only external force assumed to be acting on the thin film liquid is gravity g. Thin film flows on the rotating discs, like other flows, should also satisfy the continuity condition, which states the law of conservation of mass and again expressed in cylindrical coordinates [9]

$$\frac{1}{r}\left[\frac{\partial}{\partial r}(ru_r)\right]+\frac{1}{r}\frac{\partial u_\theta}{\partial \theta}+\frac{\partial u_z}{\partial z}=0 \tag{2}$$

2.2. Boundary conditions and simplifications

At the surface of the disc, i.e. $z=0$, the no-slip boundary condition is imposed and the disc surface is assumed to be impermeable. As the sides of the disc are symmetrical, only one side is considered here. Flow on the rim of the disc will be discussed later. Thus,

$$u_r=0,\quad u_\theta=r\Omega,\quad u_z=0 \tag{3}$$

The total rate of change of the thin film thickness should be equal to zero, which results in the following kinematic condition [9]

$$\frac{\partial h}{\partial t} - u_z - u_r \frac{\partial h}{\partial r} - \frac{1}{r} u_\theta \frac{\partial h}{\partial \theta} \tag{4}$$

Considering the film coating on one surface of the disc, Equation (2) is integrated over the film thickness to obtain

$$u_z = -\int_0^h \left\{ \frac{1}{r} \left[\frac{\partial}{\partial r} (r\, u_r) \right] + \frac{1}{r} \frac{\partial u_\theta}{\partial \theta} \right\} dz$$

Applying the Leibniz integration rule [17] yields

$$u_z = -\frac{1}{r} \left[\frac{\partial}{\partial r} \left(r \int_0^h u_r \, dz \right) \right] + u_r \frac{\partial h}{\partial r} - \frac{1}{r} \frac{\partial}{\partial \theta} \left(\int_0^h u_\theta \, dz \right) + \frac{1}{r} \frac{\partial h}{\partial \theta}$$

On comparison of this expression with Equation (4)

$$\frac{\partial h}{\partial t} = -\frac{1}{r} \left[\frac{\partial}{\partial r} \left(r \int_0^h u_r dz \right) \right] - \frac{1}{r} \frac{\partial}{\partial \theta} \left(\int_0^h u_\theta dz \right) \tag{5}$$

is obtained.

At the thin film surface, $z = h(r, \theta, t)$, the static pressure should balance the surface tension force, which requires the normal stress condition to satisfy,

$$\hat{n}\, \Pi\, \hat{n} = 2\sigma k \tag{6}$$

Here Π is the stress tensor. While at the interface of the free surface, if the friction due to the induced air flow is neglected, the tangential stresses on the free surface of the film should disappear, giving

$$\hat{n}\,\Pi\hat{t}_i = 0 \qquad (i-1,2) \tag{7}$$

Given that the local film thickness is known, the normal and tangential vectors in radial and angular direction can be determined [12].

$$\hat{n} = \frac{\left(-\frac{\partial h}{\partial r}, -\frac{1}{r}\frac{\partial h}{\partial \theta}, 1\right)}{\left(1+(\frac{\partial h}{\partial r})^2 + \frac{1}{r^2}(\frac{\partial h}{\partial \theta})^2\right)^{1/2}}, \quad \hat{t}_1 = \frac{\left(1, 0, \frac{\partial h}{\partial r}\right)}{\left(1+(\frac{\partial h}{\partial r})^2\right)^{1/2}}, \quad \hat{t}_2 = \frac{\left(0, 1, \frac{1}{r}\frac{\partial h}{\partial \theta}\right)}{\left(1+\frac{1}{r^2}(\frac{\partial h}{\partial \theta})^2\right)^{1/2}} \tag{8}$$

The stress tensor Π is defined and given by [12].

$$\Pi = \begin{pmatrix} \Pi_{rr} & \Pi_{r\theta} & \Pi_{rz} \\ \Pi_{\theta r} & \Pi_{\theta\theta} & \Pi_{\theta z} \\ \Pi_{zr} & \Pi_{z\theta} & \Pi_{zz} \end{pmatrix} =$$

$$\begin{pmatrix} -p+2\mu\frac{\partial u_r}{\partial r} & \mu\left(\frac{1}{r}\frac{\partial u_r}{\partial \theta}+\frac{\partial u_\theta}{\partial r}-\frac{u_\theta}{r}\right) & \mu\left(\frac{\partial u_z}{\partial r}+\frac{\partial u_r}{\partial z}\right) \\ \mu\left(\frac{1}{r}\frac{\partial u_r}{\partial \theta}+\frac{\partial u_\theta}{\partial r}-\frac{u_\theta}{r}\right) & -p+2\mu\left(\frac{1}{r}\frac{\partial u_\theta}{\partial \theta}+\frac{u_r}{r}\right) & \mu\left(\frac{\partial u_\theta}{\partial z}+\frac{1}{r}\frac{\partial u_z}{\partial \theta}\right) \\ \mu\left(\frac{\partial u_z}{\partial r}+\frac{\partial u_r}{\partial z}\right) & \mu\left(\frac{\partial u_\theta}{\partial z}+\frac{1}{r}\frac{\partial u_z}{\partial \theta}\right) & -p+2\mu\frac{\partial u_z}{\partial z} \end{pmatrix} \tag{9}$$

The surface tension σ is almost unchanged and assumed to be constant. From this, the mean curvature of the thin film free surface can be estimated by

$$k = \frac{1}{2}\left(\frac{1}{r}\frac{\partial}{\partial r}\frac{r\frac{\partial h}{\partial r}}{\left(1+\left(\frac{\partial h}{\partial r}\right)^2+\frac{1}{r^2}\left(\frac{\partial h}{\partial \theta}\right)^2\right)^{\frac{1}{2}}}+\frac{1}{r}\frac{\partial}{\partial \theta}\frac{\frac{1}{r}\frac{\partial h}{\partial \theta}}{\left(1+\left(\frac{\partial h}{\partial r}\right)^2+\frac{1}{r^2}\left(\frac{\partial h}{\partial \theta}\right)^2\right)^{\frac{1}{2}}}\right) \tag{10}$$

The boundary conditions are found by substituting equations (9) and (10) into (6) and (7).

The boundary conditions for the normal stress is

$$-p+\frac{2\mu}{1+(\frac{\partial h}{\partial r})^2+\frac{1}{r^2}(\frac{\partial h}{\partial \theta})^2}\left\{\begin{array}{l}\left(\frac{1}{r}\frac{\partial u_r}{\partial \theta}+\frac{\partial u_\theta}{\partial r}-\frac{u_\theta}{r}\right)\frac{1}{r}\frac{\partial h}{\partial r}\frac{\partial h}{\partial \theta}-\left(\frac{\partial r_z}{\partial r}+\frac{\partial u_r}{\partial z}\right)\frac{\partial h}{\partial r}\quad\left(\frac{\partial u_\theta}{\partial z}+\frac{1}{r}\frac{\partial u_z}{\partial \theta}\right)\frac{1}{r}\frac{\partial h}{\partial \theta}\\+\frac{\partial u_r}{\partial r}(\frac{\partial h}{\partial r})^2+\left(\frac{\partial u_\theta}{\partial \theta}+u_r\right)\frac{1}{r^3}(\frac{\partial h}{\partial \theta})^2+\frac{\partial u_z}{\partial z}\end{array}\right\}$$

$$=\sigma\left[\frac{1}{r}\frac{\partial}{\partial r}\left\{\frac{r\frac{\partial h}{\partial r}}{\left(1+(\frac{\partial h}{\partial r})^2+\frac{1}{r^2}(\frac{\partial h}{\partial \theta})^2\right)^{\frac{1}{2}}}\right\}+\frac{1}{r}\frac{\partial}{\partial \theta}\left\{\frac{\frac{1}{r}\frac{\partial h}{\partial \theta}}{\left(1+(\frac{\partial h}{\partial r})^2+\frac{1}{r^2}(\frac{\partial h}{\partial \theta})^2\right)^{\frac{1}{2}}}\right\}\right] \tag{11}$$

the tangential stress condition in the radial direction is

$$\begin{array}{l}2\left(\frac{\partial u_z}{\partial z}-\frac{\partial u_r}{\partial r}\right)\frac{\partial h}{\partial r}-\left(\frac{1}{r}\frac{\partial u_r}{\partial \theta}+\frac{\partial u_\theta}{\partial r}-\frac{u_\theta}{r}\right)\frac{1}{r}\frac{\partial h}{\partial \theta}+\\\left(\frac{\partial u_z}{\partial r}+\frac{\partial u_r}{\partial z}\right)\left(1-(\frac{\partial h}{\partial r})^2\right)-\left(\frac{\partial u_\theta}{\partial z}+\frac{1}{r}\frac{\partial u_z}{\partial \theta}\right)\frac{1}{r}\frac{\partial h}{\partial r}\frac{\partial h}{\partial \theta}=0\end{array} \tag{12}$$

and the tangential stress condition in the angular direction is

$$\begin{array}{l}2\left(\frac{\partial u_z}{\partial z}-\frac{1}{r}\frac{\partial u_\theta}{\partial \theta}-\frac{u_r}{r}\right)\frac{1}{r}\frac{\partial h}{\partial \theta}-\left(\frac{1}{r}\frac{\partial u_r}{\partial \theta}+\frac{\partial u_\theta}{\partial r}-\frac{u_\theta}{r}\right)\frac{\partial h}{\partial r}+\\\left(\frac{\partial u_\theta}{\partial z}+\frac{1}{r}\frac{\partial u_z}{\partial \theta}\right)\left(1-\frac{1}{r^2}(\frac{\partial h}{\partial \theta})^2\right)-\left(\frac{\partial u_z}{\partial r}+\frac{\partial u_r}{\partial z}\right)\frac{1}{r}\frac{\partial h}{\partial r}\frac{\partial h}{\partial \theta}=0\end{array} \tag{13}$$

The direct solution of the Navier-Stokes equation together with the boundary conditions (3), (6), and (7) coupled with Equation (5), is impractical since the equations involved are highly non-linear, however, a numerical solution would be feasible.

2.3. Nondimensional analysis

This section will discuss the existing analysis for the thin film flows on a vertically rotational disc [9] to such problem, which will be used for guidance for CFD modelling of the thin film flow on the vertically rotating disc.

For the film formation on the vertically rotating disc, the use of the lubrication approximation [9] is feasible but the appropriate length scale should be considered. The typical length scale should be R, the radius of the disc, while the tangential velocity of the rotating disc, U, may be the suitable characteristic velocity scale, which is given by

$$U = R\Omega \tag{14}$$

and the time scale is chosen as

$$T = R/U \tag{15}$$

Since the liquid film formed on the surface of the rotating disc is very thin [9, 18] a small parameter in the analysis can be introduced, i.e.

$$\alpha = \frac{H}{R} << 1 \tag{16}$$

On this basis, the following dimensionless variables can be introduced:

$$r = R\hat{r},\ O = \hat{O},\ z = H\hat{z},\ u_r = U\hat{u}_r,\ u_\theta = U\hat{u}_\theta,\ u_z = \alpha U\hat{u}_z,\ p = P\hat{p},\ t = T\hat{t} \tag{17}$$

The dominant viscous term is balanced with gravitational term in the u_r-momentum equation so that the characteristic height H can be scaled, which yields

$$H = \sqrt{\frac{\mu U}{\rho g}} \tag{18}$$

It is expected that the pressure will compete with the dominant viscous term, so that

$$P = \frac{\mu U / R}{H^2} \tag{19}$$

Because the thin film involves the free surface, the surface tension plays an important role in controlling the liquid surface. The following scale can be used to relate to the normal stress boundary condition, i.e.

$$P = \frac{\sigma H}{R^2} \tag{20}$$

Equating Equations (19) and (20) gives the scale for R as

$$R = \frac{H}{\left(\frac{\mu U}{\sigma}\right)^{1/3}} \tag{21}$$

When the capillary number Ca is introduced, it can be shown that Ca is small for the case of the thin film flow on the vertically rotating disc.

$$Ca = \left(\frac{\mu U}{\sigma}\right) = \left(\frac{H}{R}\right)^3 << 1 \tag{22}$$

It is noted that this length scale is appropriate for the thin film region away from the liquid bath. The length scale should be reconsidered for the balance of gravity and surface tension forces.

$$P = \rho g R \tag{23}$$

The pressure scale can be determined by surface tension

$$P = \sqrt{\sigma \rho g} \tag{24}$$

From equations (23) and (24) the length scale near the liquid bath can be obtained

$$R = \left(\frac{\sigma}{\rho g} \right)^{\frac{1}{2}} \tag{25}$$

We also define a Reynolds number, $Re = \rho UR/\mu$, non-dimensionalising Equation (1) yields

$$\begin{aligned} &\alpha^2 \mathrm{Re}\left[\frac{\partial \hat{u}_r}{\partial \hat{t}} + \hat{u}_r \frac{\partial u_r}{\partial \hat{r}} + \frac{\hat{u}_\theta}{\hat{r}} \frac{\partial \hat{u}_r}{\partial \hat{\theta}} - \frac{\hat{u}_\theta^2}{\hat{r}} + \hat{u}_z \frac{\partial \hat{u}_r}{\partial \hat{z}} \right] = -\frac{\partial \hat{p}}{\partial \hat{r}} + \frac{\partial \hat{u}_r^2}{\partial \hat{z}^2} \\ &-\sin\hat{\theta} + \alpha^2 \left[\frac{1}{\hat{r}} \frac{\partial}{\partial \hat{r}} \left(\hat{r} \frac{\partial \hat{u}_r}{\partial \hat{r}} \right) + \frac{1}{\hat{r}^2} \frac{\partial^2 \hat{u}_r}{\partial \hat{\theta}^2} - \frac{2}{\hat{r}^2} \frac{\partial \hat{u}_\theta}{\partial \hat{\theta}} - \frac{\hat{u}_r}{\hat{r}^2} \right] \end{aligned} \tag{26}$$

$$\begin{aligned} &\alpha^2 \mathrm{Re}\left[\frac{\partial \hat{u}_\theta}{\partial \hat{t}} + \hat{u}_r \frac{\partial \hat{u}_\theta}{\partial \hat{r}} + \frac{\hat{u}_\theta}{\hat{r}} \frac{\partial \hat{u}_\theta}{\partial \hat{\theta}} + \frac{\hat{u}_r \hat{u}_\theta}{\hat{r}} + \hat{u}_z \frac{\partial \hat{u}_\theta}{\partial \hat{z}} \right] = -\frac{1}{\hat{r}} \frac{\partial \hat{p}}{\partial \hat{\theta}} + \frac{\partial \hat{u}_\theta^2}{\partial \hat{z}^2} \\ &-\cos\hat{\theta} + \alpha^2 \left[\frac{1}{\hat{r}} \frac{\partial}{\partial \hat{r}} \left(\hat{r} \frac{\partial \hat{u}_\theta}{\partial \hat{r}} \right) + \frac{1}{\hat{r}^2} \frac{\partial \hat{u}_\theta^2}{\partial \hat{\theta}^2} + \frac{2}{\hat{r}^2} \frac{\partial \hat{u}_r}{\partial \hat{\theta}} - \frac{\hat{u}_\theta}{\hat{r}^2} \right] \end{aligned} \tag{27}$$

$$\begin{aligned} &\alpha^4 \mathrm{Re}\left[\frac{\partial \hat{u}_z}{\partial \hat{t}} + \hat{u}_r \frac{\partial \hat{u}_z}{\partial \hat{r}} + \frac{\hat{u}_\theta}{\hat{r}} \frac{\partial \hat{u}_\theta}{\partial \hat{\theta}} + \hat{u}_z \frac{\partial \hat{u}_z}{\partial \hat{z}} \right] = -\frac{\partial \hat{p}}{\partial \hat{z}} + \alpha^2 \frac{\partial \hat{u}_z^2}{\partial \hat{z}^2} \\ &+ \alpha^4 \left[\frac{1}{\hat{r}} \frac{\partial}{\partial \hat{r}} \left(\hat{r} \frac{\partial \hat{u}_z}{\partial \hat{r}} \right) + \frac{1}{\hat{r}^2} \frac{\partial \hat{u}_z^2}{\partial \hat{\theta}^2} \right] \end{aligned} \tag{28}$$

Here all variables have been non-dimensionalised.

2.4. Derivation of simplified equation for film thickness approximation

Because α is very small, Equations (26), (27) and (28) can be simplified as

$$0 = -\frac{\partial \hat{p}}{\partial \hat{r}} + \frac{\partial^2 \hat{u}_r}{\partial \hat{z}^2} - \sin\hat{\theta} \tag{29}$$

$$0 = -\frac{1}{\hat{r}}\frac{\partial \hat{p}}{\partial \hat{\theta}} + \frac{\partial^2 \hat{u}_\theta}{\partial \hat{z}^2} - \cos\hat{\theta} \tag{30}$$

$$0 = -\frac{\partial \hat{p}}{\partial \hat{z}} \tag{31}$$

It can be seen from Equation (31) that p does not depend on z. The boundary conditions at the disc surface, $\hat{z} = 0$, are

$$\hat{u}_r = 0, \quad \hat{u}_\theta = \hat{r}\hat{\Omega}, \quad \hat{u}_z = 0, \tag{32}$$

The boundary conditions at the free liquid surface $\hat{z} = \hat{h}(\hat{r}, \hat{\theta}, \hat{t})$, has been non-dimensionalised as:

$$-\hat{p} + \frac{2\alpha^2}{1+\alpha^2\frac{\partial^2\hat{h}}{\partial\hat{r}^2} + \frac{\alpha^2}{\hat{r}^2}\frac{\partial^2\hat{h}}{\partial\hat{\theta}^2}} \left\{ \begin{array}{l} \alpha^2\left(\frac{1}{\hat{r}}\frac{\partial\hat{u}_r}{\partial\hat{\theta}} + \frac{\partial\hat{u}_\theta}{\partial\hat{r}} - \frac{\hat{u}_\theta}{\hat{r}}\right)\frac{1}{r}\frac{\partial\hat{h}}{\partial\hat{r}}\frac{\partial\hat{h}}{\partial\hat{\theta}} - \left(\alpha^2\frac{\partial\hat{u}_z}{\partial\hat{r}} + \frac{\partial\hat{u}_r}{\partial\hat{z}}\right)\frac{\partial\hat{h}}{\partial\hat{r}} - \left(\frac{\partial\hat{u}_z}{\partial\hat{z}} + \frac{\alpha^2}{\hat{r}}\frac{\partial\hat{u}_z}{\partial\hat{\theta}}\right) \\ \frac{1}{r}\frac{\partial\hat{h}}{\partial\hat{\theta}} + \alpha^2\frac{\partial\hat{u}_r}{\partial\hat{r}}\frac{\partial^2\hat{h}}{\partial\hat{r}^2} + \alpha^2\left(\frac{\partial\hat{u}_\theta}{\partial\hat{\theta}} + \hat{u}_r\right)\frac{1}{\hat{r}^3}\frac{\partial^2\hat{h}}{\partial\hat{\theta}^2} + \frac{\partial\hat{u}_z}{\partial\hat{z}} \end{array} \right\}$$

$$= \frac{1}{\hat{r}}\frac{\partial}{\partial\hat{r}}\left\{\frac{\hat{r}\frac{\partial\hat{h}}{\partial\hat{r}}}{\left(1+\alpha^2(\frac{\partial\hat{h}}{\partial\hat{r}})^2 + \frac{\alpha^2}{\hat{r}^2}(\frac{\partial\hat{h}}{\partial\hat{\theta}})^2\right)^{\frac{1}{2}}}\right\} + \frac{1}{\hat{r}}\frac{\partial}{\partial\hat{\theta}}\left\{\frac{\frac{1}{\hat{r}}\frac{\partial\hat{h}}{\partial\hat{\theta}}}{\left(1+\alpha^2(\frac{\partial\hat{h}}{\partial\hat{r}})^2 + \frac{\alpha^2}{\hat{r}^2}(\frac{\partial\hat{h}}{\partial\hat{\theta}})^2\right)^{\frac{1}{2}}}\right\} \tag{33}$$

$$2\alpha^2\left(\frac{\partial\hat{u}_z}{\partial\hat{z}} - \frac{\partial\hat{u}_r}{\partial\hat{r}}\right)\frac{\partial\hat{h}}{\partial\hat{r}} - \alpha^2\left(\frac{1}{\hat{r}}\frac{\partial\hat{u}_r}{\partial\hat{\theta}} + \frac{\partial\hat{u}_\theta}{\partial\hat{r}} - \frac{\hat{u}_\theta}{\hat{r}}\right)\frac{1}{\hat{r}}\frac{\partial\hat{h}}{\partial\hat{\theta}} +$$
$$\left(\alpha^2\frac{\partial\hat{u}_z}{\partial\hat{r}} + \frac{\partial\hat{u}_r}{\partial\hat{z}}\right)\left(1 - \alpha^2\frac{\partial^2\hat{h}}{\partial\hat{r}^2}\right) - \alpha^2\left(\frac{\partial\hat{u}_\theta}{\partial\hat{z}} + \frac{\alpha^2}{\hat{r}}\frac{\partial\hat{u}_z}{\partial\hat{\theta}}\right)\frac{1}{\hat{r}}\frac{\partial\hat{h}}{\partial\hat{r}}\frac{\partial\hat{h}}{\partial\hat{\theta}} = 0 \tag{34}$$

$$2\alpha^2\left(\frac{\partial \hat{u}_z}{\partial \hat{z}}-\frac{1}{\hat{r}}\frac{\partial \hat{u}_\theta}{\partial \hat{\theta}}-\frac{\hat{u}_r}{\hat{r}}\right)\frac{1}{\hat{r}}\frac{\partial \hat{h}}{\partial \hat{\theta}}-\alpha^2\left(\frac{1}{\hat{r}}\frac{\partial \hat{u}_r}{\partial \hat{\theta}}+\frac{\partial \hat{u}_\theta}{\partial \hat{r}}-\frac{\hat{u}_\theta}{\hat{r}}\right)\frac{\partial \hat{h}}{\partial \hat{r}}+$$
$$\left(\frac{\partial \hat{u}_\theta}{\partial \hat{z}}+\frac{\alpha^2}{\hat{r}}\frac{\partial \hat{u}_z}{\partial \hat{\theta}}\right)\left(1-\frac{\alpha^2}{\hat{r}^2}\frac{\partial^2 \hat{h}}{\partial \hat{\theta}^2}\right)-\alpha^2\left(\alpha^2\frac{\partial \hat{u}_z}{\partial \hat{r}}+\frac{\partial \hat{u}_r}{\partial \hat{z}}\right)\frac{1}{\hat{r}}\frac{\partial \hat{h}}{\partial \hat{r}}\frac{\partial \hat{h}}{\partial \hat{\theta}}=0 \quad (35)$$

The conditions (33), (34) and (35) can be simplified as

$$\hat{p}=\frac{1}{\hat{r}}\frac{\partial}{\partial \hat{r}}\left(\hat{r}\frac{\partial \hat{h}}{\partial \hat{r}}\right)+\frac{\partial^2 \hat{h}}{\hat{r}^2\partial \hat{\theta}^2} \quad (\hat{z}=\hat{h}) \quad (36)$$

$$\frac{\partial \hat{u}_r}{\partial \hat{z}}=0 \quad (\hat{z}=\hat{h}) \quad (37)$$

$$\frac{\partial \hat{u}_\theta}{\partial \hat{z}}=0 \quad (\hat{z}=\hat{h}) \quad (38)$$

Equations (33), (34) and (35), coupled with the kinematic condition for description of the thin film free surface, can now be solved with the boundary conditions (36), (37) and (38). The kinematic condition given in Equation (5) is non-dimensionalised as

$$\frac{\partial \hat{h}}{\partial \hat{t}}=-\frac{1}{\hat{r}}\frac{\partial}{\partial \hat{r}}\left(\hat{r}\int_0^{\hat{h}}\hat{u}_r d\hat{z}\right)-\frac{1}{\hat{r}}\frac{\partial}{\partial \hat{\theta}}\left(\int_0^{\hat{h}}\hat{u}_\theta d\hat{z}\right) \quad (39)$$

The velocity components u_r and u_θ are determined first, and then the film thickness can be found through equation (39).

Rearranging Equations (29) and (30) gives,

$$\frac{\partial^2 \hat{u}_r}{\partial \hat{z}^2}=\frac{\partial \hat{p}}{\partial \hat{r}}+\sin\hat{\theta} \quad (40)$$

$$\frac{\partial^2 \hat{u}_\theta}{\partial \hat{z}^2} = \frac{1}{\hat{r}} \frac{\partial \hat{p}}{\partial \hat{\theta}} + \cos\hat{\theta} \tag{41}$$

Integration twice of Equation (40) and (41) with respect to z and substitution of $\hat{u}_r$ and $\hat{u}_\theta$ into Equation (39) and integrating again over the film thickness by applying boundary conditions (32), (37), (38), gives

$$\frac{\partial \hat{h}}{\partial \hat{t}} = \frac{1}{\hat{r}} \frac{\partial}{\partial \hat{r}} \left[\hat{r} \frac{h^3}{3} \left(\frac{\partial \hat{p}}{\partial \hat{r}} + \sin\hat{\theta} \right) \right] + \frac{1}{\hat{r}} \frac{\partial}{\partial \hat{\theta}} \left[\frac{h^3}{3} \left(\frac{1}{\hat{r}} \frac{\partial \hat{p}}{\partial \hat{\theta}} + \cos\hat{\theta} \right) - \hat{\Omega} \hat{r} \hat{h} \right] \tag{42}$$

Equation (42) is the standard equation for film thickness [9], where

$$\hat{\Omega} = \frac{\mu \Omega}{\sqrt{\rho g \sigma}}$$

It should be noted that boundary conditions (36) to (38) is only appropriate far away from the liquid bath. If the length scale is reconsidered in the vicinity of the liquid bath, as shown in Equation (25) based on the analysis by Afanasiev *et al.* [9], then boundary condition (36) becomes

$$-\hat{p} = \frac{1}{\hat{r}} \frac{\partial}{\partial \hat{r}} \frac{\hat{r} \frac{\partial \hat{h}}{\partial \hat{r}}}{\left(1 + (\frac{\partial \hat{h}}{\partial \hat{r}})^2 + \frac{1}{r^2} (\frac{\partial \hat{h}}{\partial \hat{\theta}})^2 \right)^{\frac{1}{2}}} + \frac{1}{\hat{r}} \frac{\partial}{\partial \hat{\theta}} \frac{\frac{1}{\hat{r}} \frac{\partial \hat{h}}{\partial \hat{\theta}}}{\left(1 + (\frac{\partial \hat{h}}{\partial \hat{r}})^2 + \frac{1}{r^2} (\frac{\partial \hat{h}}{\partial \hat{\theta}})^2 \right)^{\frac{1}{2}}} \quad (\hat{z} = \hat{h}) \tag{43}$$

For the scaling near the liquid bath, the distance in the z-direction ($\hat{z}$) is taken equal to the film thickness ($\hat{h}$).

Surface tension force has a significant influence on the film thickness profile, so Equation (42) should be solved in conjunction with Equation (43), From Equation (43) and (10) $\hat{p} = -2k$, where k is curvature of the free surface. Substituting this value in Equation (42) gives,

$$\frac{\partial \hat{h}}{\partial \hat{t}} = \frac{1}{\hat{r}}\frac{\partial}{\partial \hat{r}}\left[-\hat{r}\frac{2\hat{h}^3}{3}\left(\frac{\partial k}{\partial \hat{r}} + \sin\hat{\theta}\right)\right] + \frac{1}{\hat{r}}\frac{\partial}{\partial \hat{\theta}}\left[-\frac{2\hat{h}^3}{3}\left(\frac{1}{\hat{r}}\frac{\partial k}{\partial \hat{\theta}} + \cos\hat{\theta}\right) - \hat{\Omega}\hat{r}\hat{h}\right] \tag{44}$$

Equation (44) is a simplified equation for film thickness approximation, which is a new result. The film thickness can be estimated using this equation, based on the approximation of the curvature of the free surface. Equation (44) is non-linear, and must be solved numerically. For steady thin film flow, $\frac{\partial \hat{h}}{\partial \hat{t}} = 0$ so the RHS of Equation (44) is zero.

3. CFD modelling of the thin film flow on a vertically rotating disc

The use of a high quality mesh and reasonable boundary conditions which are incorporated into CFD modelling is crucial to this study [19, 20]. For the numerical solution of the thin film free surface flow, CFD code - Fluent has been used.

A full three dimensional model of the rotating disc was constructed, using a rotating cylindrical coordinate system to model the rotating disc feature. The model dimensions have been chosen following the work done by Afanasiev *et al.* [9]: the disc radius has been taken to be $R = 27.23$ mm and the thickness of the disc to be 1 mm. The size of the cylindrical vessel should be large enough that the walls are far enough from the disc so as to ensure that the boundary condition, $\frac{\partial}{\partial z} = 0$ can be imposed when the vessel is partially filled with liquid. To achieve this, the cylindrical vessel was specified to have a diameter of 80 mm and a length of 40 mm.

From the boundary layer thickness theory [18], the flow over a flat plate of the length of 54.46 mm corresponds to a boundary layer thickness of about 0.2 mm. Also, based on the work done by Afanasiev et al., [9] , the measured film thickness is about 0.4 mm. Thus, for a vertically rotating disc of radius 27.23 mm, the thin film thickness is estimated to be 0.1~0.5 mm.

3.1. Grid generation

Since the film formed on the rotating disc is very thin, a fine mesh is required in the vicinity of the disc. A boundary layer mesh has been imposed (as shown in Figure 2a) with a minimum mesh size

of 0.025 mm on the z direction, at the surface of the disc, and morphing to 1.5 mm in the main domain. The minimum mesh size has been prescribed to give at least one quarter of the estimated minimum film thickness, so as to yield at least 4 cells within the film and thereby to improve the accuracy of the film thickness prediction from the numerical simulations.

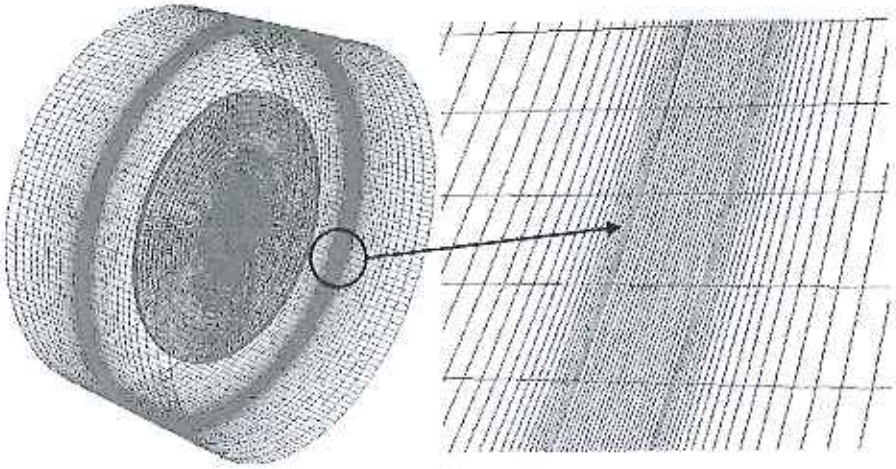

Figure 2a. Boundary layer mesh

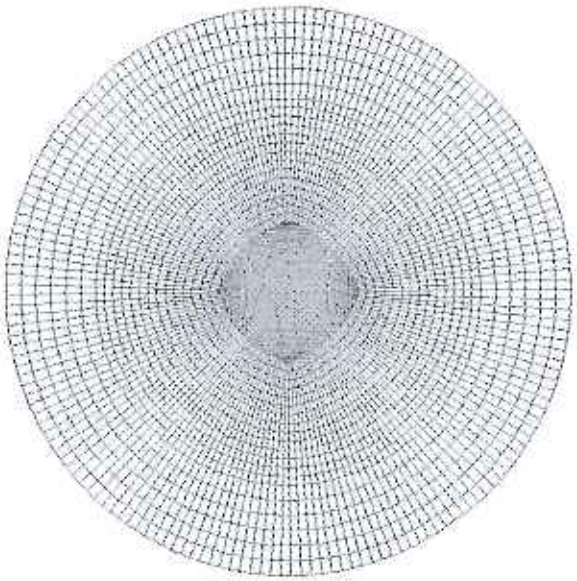

Figure 2b. Grid generation on the disc surface

A structured grid with hexahedral cells was generated with map face meshes on the circular surfaces as shown in Figure 2b, and extended by the Cooper [21] volume mesh to avoid numerical diffusion as much as possible. The use of a refined mesh [22] was tested varying the number of elements in the model (596,432; 482,653 and 369,714). In each case the simulation results obtained were similar, and so deemed to be independent of the mesh. The total number of elements used in the subsequent CFD modelling is 369,714.

3.2. VOF demonstration

The Volume of Fluid method (VOF) has been recognised as an appropriate numerical technique for tracking and locating the free surface of two or more immiscible fluids. This works by calculating the volume fractions in each cell of a fixed Eulerian grid [23]. A volume fraction parameter F for each of the Eulerian grid is defined in the VOF method. A cell is assumed to be completely filled with liquid when $F=1$, empty when $F=0$, and it contains a mixture of two or more phases if $0<F<1$. The function F can be determined by using the following advection equation.

$$\frac{\partial F}{\partial t}+U.\nabla F=0$$

Clearly, the choice of Eulerian grid size will determine the precision in modelling of the film surface area. In turn, the film surface area determines the film surface tension. In this study, typical cell sizes for the cells for which 0<F<1 were $\sim 2.5\times10^{-2}$ mm, meaning that the film surface area was captured with a precision of ~1 x 10^{-3} mm^2, and the surface tension with a precision of ~1 x 10^{-7} Nmm^{-2}. Based on F values, the free surface shape can be determined using a particular interpolation technique [24]. In the current study the VOF method is employed to determine the local thickness of the thin film on the vertically rotating disc, as a function of radial and angular position.

3.3. Transient analysis considerations

One important application of the VOF method is for transient simulation, i.e. unsteady flow simulation. In this case a careful selection of the time step is required to ensure that the simulation

is numerically stable. The criterion used for determining the time step is based on the Courant number [25] and demands that the free surface flow front advance must not exceed a mesh interval. This Courant-Friedrichs-Lewy condition (CFL) is a necessary condition [26] for convergence while solving certain partial differential equations numerically. The CFL condition is expressed as

$$\frac{U.\Delta t}{\Delta x} \leq C \tag{46}$$

where U is the liquid velocity, Δt is the time step and Δx is the mesh interval or mesh size. As, $U\Delta t < \Delta x$ should be ensured in all unsteady simulation to keep stability, in this case, Equation (46) gives a minimum time step about 10^{-3} s.

4. Numerical results and discussions

The CFD simulations have been conducted four different liquids of different viscosities as shown in Table 1. In order to compare simulation results, the properties of the test liquid have been taken from Afanasiev *et. al.* [9]. Three types of PDMS (Polydimethylsiloxane) liquids of different viscosities have been taken.

Table 1. Properties of the liquids used in the simulations

	μ (Pa.s)	σ (N/m)	ρ (kg/m^3)
Test fluid	1	0.0727	1000
PDMS-1	1	0.0211	975
PDMS-2	5	0.0211	975
PDMS-3	10	0.0211	975

In the simulations, the disc is assumed to rotate at different angular velocities (Ω 1,2,3 and 6 rpm) while it is immersed in liquid (d' = 0,0.25 and 0.5): the immersion depth d is non-dimensionalised here by dividing with the radius of the disc.

In the work by Afanasiev *et. al.* [9], the film thickness profile is the only function of r, however, our CFD simulation results have clearly indicated that the actual film thickness is not only dependent on r but also on θ.

For the case of liquid being dragged out of a bath pool on a vertical, upward moving flat plate, Landau and Levich [7] have showed that if the capillary number Ca is small, the film thickness can be estimated by

$$h = 0.93\left(\frac{\mu U}{\rho g}\right)^{1/2}(Ca)^{1/6} \tag{47}$$

where h is the film thickness, U is the velocity of the plate, ρ is density, g is gravitational force and μ is the dynamic viscosity of the liquid. Wilson [8] indicated that the approximate solution given by Landau and Levich [7] is only valid when the capillary number approaches to zero and he obtained a general solution of the film thickness when the flat plate is vertically aligned, which is expressed

$$h = \left(\frac{\mu U}{\rho g}\right)^{1/2}\left[0.94581(Ca)^{1/6} - 0.10685(Ca)^{1/2}\right] \tag{48}$$

By using similar analysis for thin flow on vertically rotating disc, Afanasiev *et. al.*[9] obtained a steady state solution of the film thickness, which is given by

$$h = 0.94581\left(\frac{\mu r\Omega}{\sqrt{\rho g\sigma}}\right)^{2/3} \tag{49}$$

The dimensionless radius of the rotating disc is taken as $R' = 10$.

The comparisons are shown at $R' = 9, 7, 5$ and 3. The film formation can be characterised by two regions, when the disc is half immersed in liquid (indicated in Figure 3), $0^0 < \theta < 90^0$ as the

region for the film drag out and $90^0 < \theta < 180^0$ as the region for the film to be dragged in [27]. The simulation revealed that the film is thick and unstable in the drag-out point and it gradually becomes stable but has a tendency of downwards and significantly affected by all the forces acting on the film flow. The force balance may play a leading role in controlling the film flow. The forces such as viscous force, inertia, gravitational force and surface tension force acting on the film flow on the rotating disc have been discussed by [28-30]. It has been indicated from the simulation that the viscous force is dominant in the drag-out region while the gravitational force is dominant in the drag-in region.

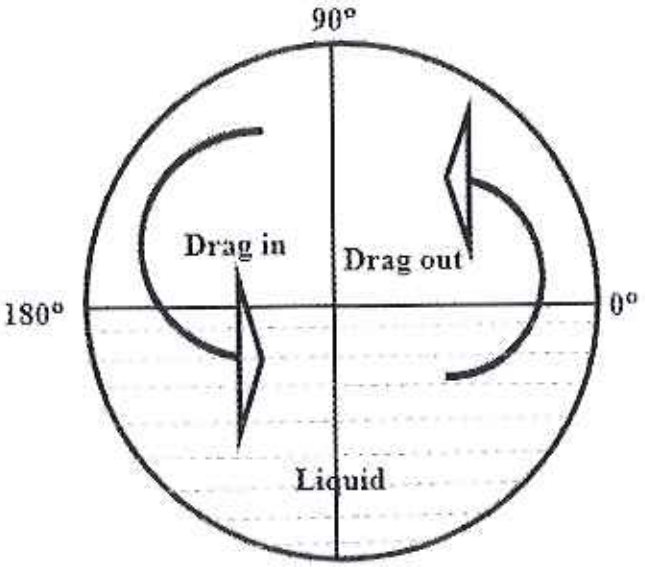

Figure 3. Schematic showing the "drag out" and "drag in" regions

Vijayraghvan and Gupta [31] obtained a correlation for the film thickness formed on a vertically rotating disc partially immersed in Newtonian liquid based on their experimental results, which in the original paper reads

$$h = \frac{7.99\, Ca^{2.93}\, \eta^{0.15}\, \Re^{5.23}}{Cas^{3.09}\, \chi^{0.024}} \tag{50}$$

where η is dimensionless surface tension number, $\Re$ is the dimensionless depth, χ is dimensionless gravitational number and Cas is modified capillary number. It can be seen from equation (50) that the effect of angular position θ is not included in their correlation, however, our/the present CFD simulation shows that the thin film thickness profile does depend on angular position θ. It should be noted that except for the regions where the film just starts to form and re-enters the liquid, the change in the thin film thickness is not remarkable in the angular region of $15^0 < \theta < 170^0$, although a slight variation in film thickness is observed. Figure 4 shows the variations of film thickness at different angular positions for given radius. Notethat here the film thickness has been non-dimensionalised first by dividing by the radius of the disc, and then multiplying by a factor of 10. The non-dimensional film thickness thus takes a value between 0 and 10 to reflect the structure of the film patterns.

In order to correlate the simulation results, dimensional analysis was conducted. The film thickness is dependent on a number of parameters and a functional relationship may be assumed.

$$h(r,\theta) = F(\rho, \mu, \sigma, g, \Omega, t, d, r, \theta,) \tag{51}$$

where ρ is the density of the fluid, μ is the dynamic viscosity, σ is the surface tension, g is the gravitational acceleration, Ω is the rotating speed, t is the flow time, d is the immersion depth of the liquid, r is the radius, and θ is the angular position. Since previous studies on thin film flow have clearly indicated that the thin film flow can be well characterised by the following dimensionless parameters like Capillary number (Ca), Froude number (Fr), Reynolds number (Re) and Webber number (We), the functional relation (51) is assumed to be able to expressed as

$$h' = k_0 \mathrm{Re}^{k_1} Ca^{k_2} Fr^{k_3} We^{k_4} F(t) F(d) \tag{52}$$

where h' is the dimensionless film thickness, k_0, k_1, k_2, k_3, k_4 are empirical constants which can be determined from the best regression fitting to the simulation results.

The CFD simulation results as shown in Figure 5a-5d can be curve-fitted using the least square technique to minimise the total error. It has been found through the trials that a combination of exponential and polynomial curve fitting can deliver the best curve fit, which is given by

$$h_\theta = ae^{-x_1\theta} + b_0 + b_1\theta + b_2\theta^2 + b_3\theta^3 + b_4\theta^4 + ce^{x_2\theta} \tag{53}$$

where, the coefficients $x_1, x_2, a, b_0, b_1, b_2, b_3, b_4$ and c have been obtained from the CFD simulation results for any given radius. The predicted film thickness at different angular positions for given radius is now well expressed based on expression (53).

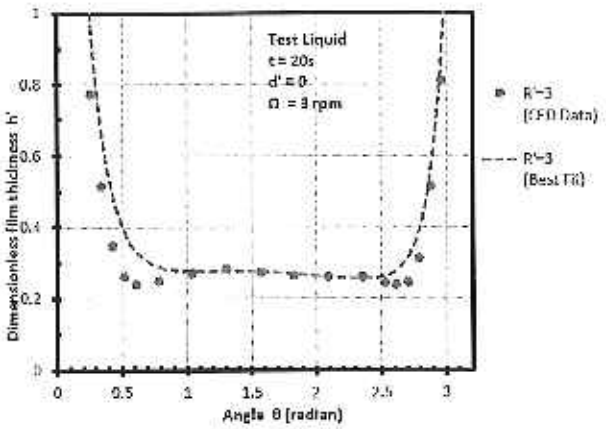

Figure 5a. Film thickness at $R' = 3$

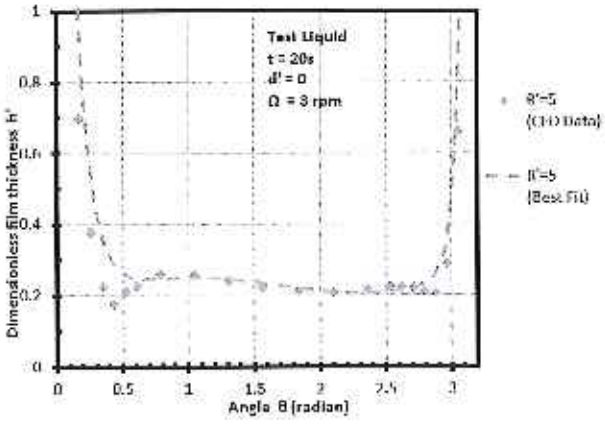

Figure 5b. Film thickness at $R' = 5$

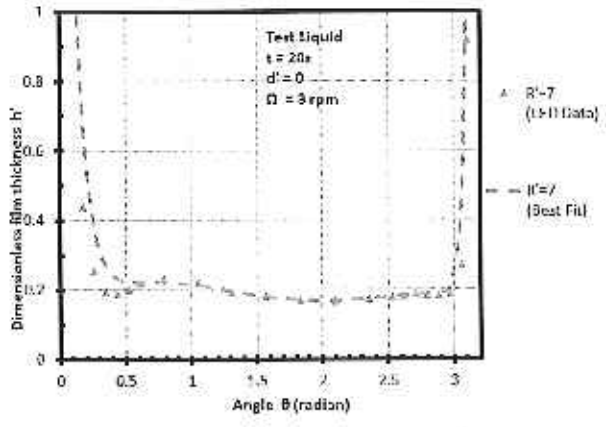

Figure 5c. Film thickness at $R' = 7$

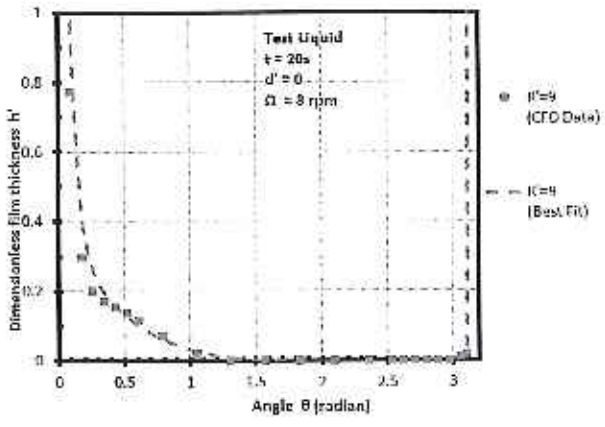

Figure 5d. Film thickness at $R' = 9$

It can be seen from Figure 5a-5d that the film thickness decreases from the central core towards the fringe of the disc. This is due to the gravitation force action which drives the film downward, however, as mentioned earlier, the film thickness varies along the circumferential direction. Based on our simulation results, the following fitted expression for a given radius $R' = 7$ is obtained, which is given by

$$h_\theta = 3.48e^{-10.63\theta} + 0.06 + 0.52\theta - 0.55\theta^2 + 0.22\theta^3 - 0.03\theta^4 + 2\times10^{-40}e^{29.48\theta} \qquad (54)$$

Equation (52) has clearly indicated that the film thickness is affected by rotational speed, which has been confirmed in our simulations, as can be seen from Figure 6. The film thickness is directly proportional to the rotating speed of the disc.

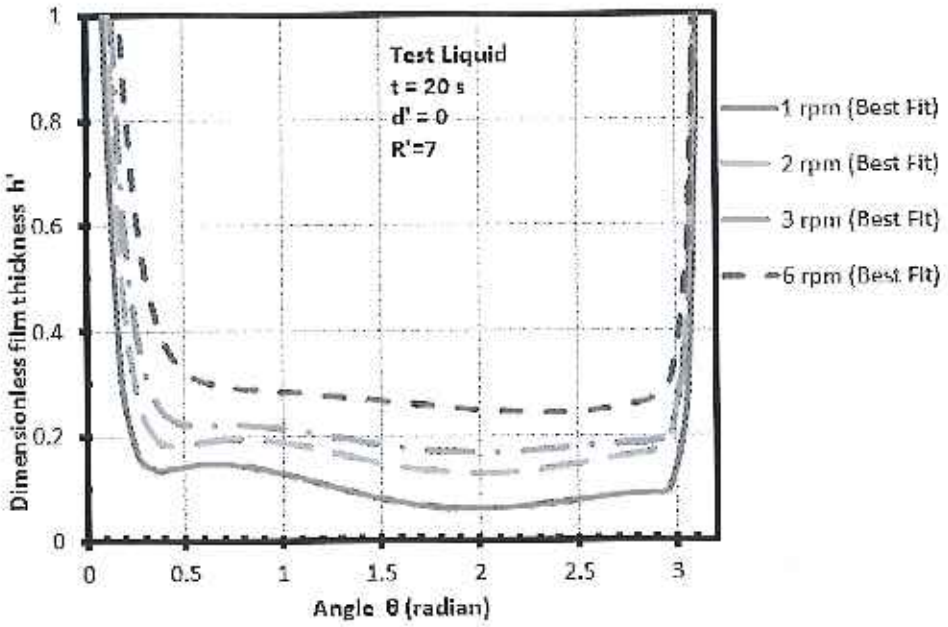

Figure 6. Film thickness at different rotational speed

There is no film formation in the centre of the rotating disk, and the film becomes very thin near the edge as the gravity is pulling down the film downwards. The film thickness increases towards the edge of the rotating disc until about $R' = 4$, before decreasing, as shown in Figure 7,

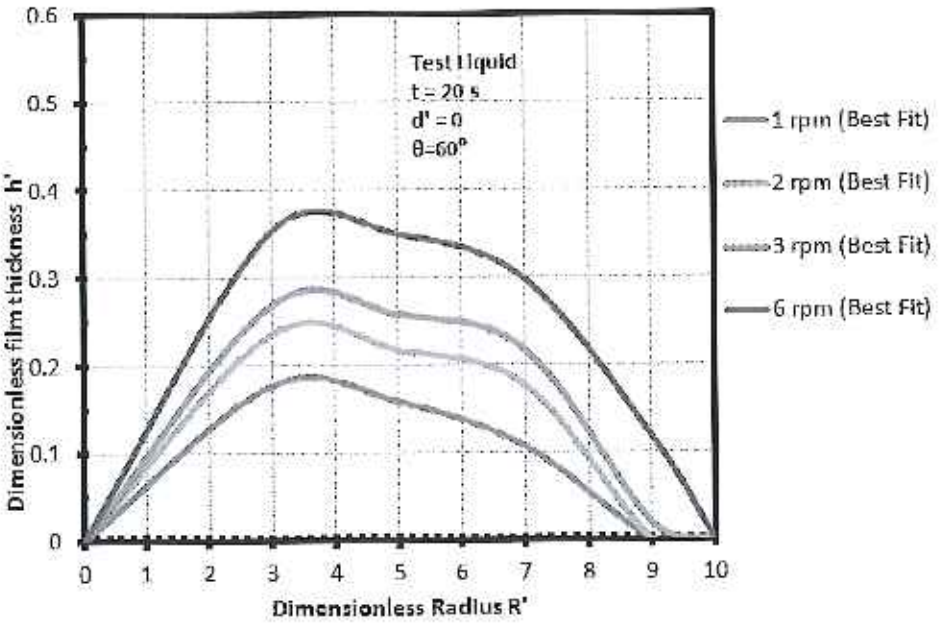

Figure 7. Film thickness at different radial positions

The influence of immersion depth on the film thickness formation was also assessed in our CFD simulations. Figure 8 shows the film thickness distributions for three different immersion depths. It is interesting to note here that except for the regions of drag-out and drag in, the film thickness only changes slightly for different immersion depths. This is in contradiction to the results as obtained by Afanasiev *et al.*, and presented in their Figure 11 [9]. One possible explanation is that the immersion depth affects only the drag in/out boundary conditions whereas the film flow on the upper part of the rotating disc depends on the overall force balance.

The film formation on the vertically rotating disc is clearly time dependent. Figure 9 shows the CFD results for the film thickness variation along the circumferential direction at given radius $R' = 7$. It can be seen from Figure 9 that the film thickness profile is almost same for a different flow duration of the liquid. When the flow duration is sufficiently long, the film flow becomes steady. Thus, for a given immersion depth, correlation (52) may be simplified as

$$h' = k_0 \,\mathrm{Re}^{k_1} Ca^{k_2} Fr^{k_3} \left(\frac{r}{R}\right)^{k_4} \theta^{k_5} \tag{55}$$

where the Webber number is $W_e = R_e \times C_a$,

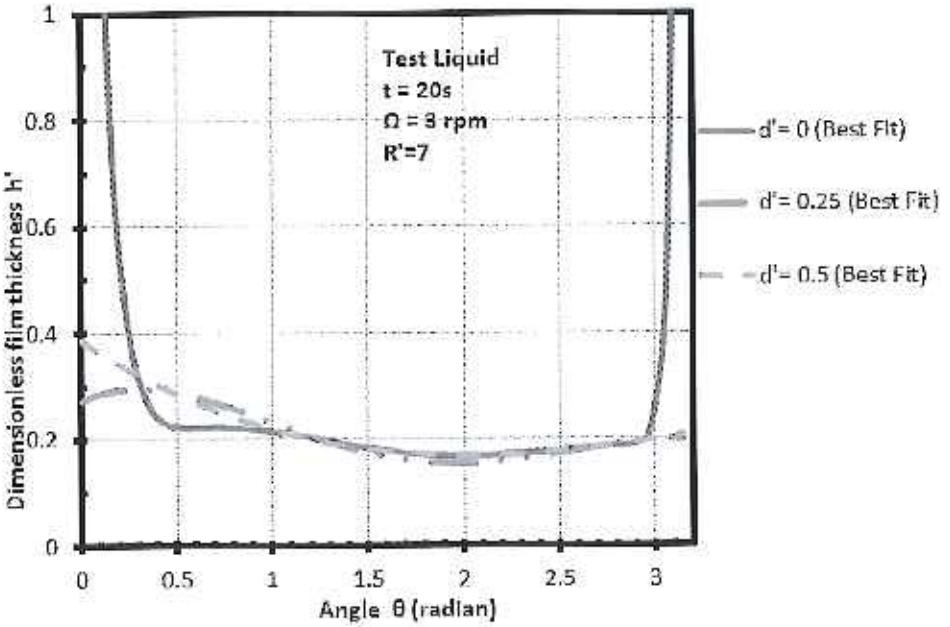

Figure 8. Film thickness at different immersion depths

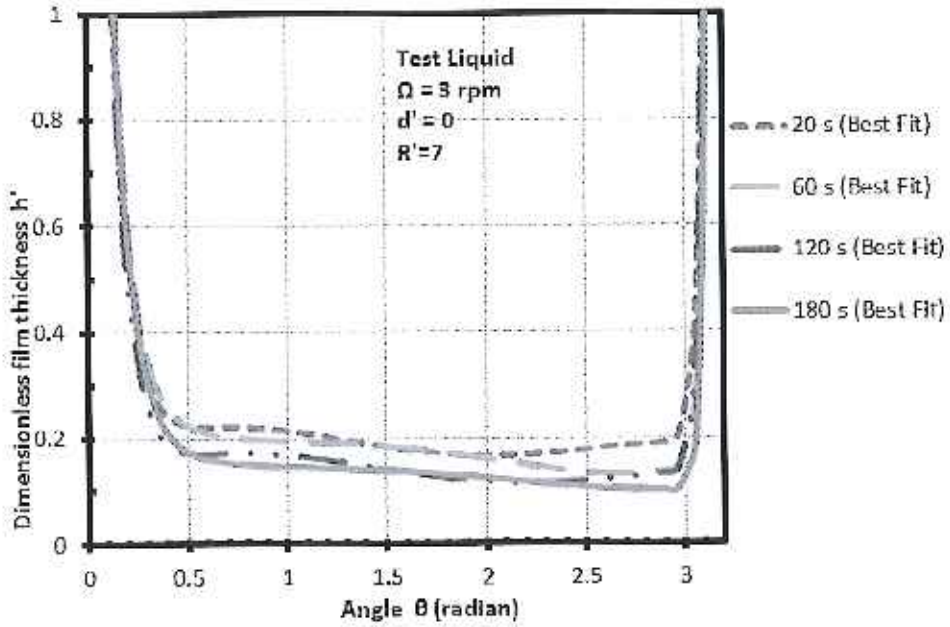

Figure 9. Film thickness at different flow time

By using correlation (55) for best fitting to the simulations, it was found that $k_0, k_1, k_2, k_3, k_4, k_5$ take the following values.

Table 2. Values of constants

Constants	Values
k_0	2.61
k_1	-0.2
k_2	0.1
k_3	0.32
k_4	0.36
k_5	-0.16

By substituting the above values into Equation (55), the calculated film thickness can be estimated by

$$h' = \frac{2.61\, Ca^{0.1} Ir^{0.32}}{\mathrm{Re}^{0.2}\left(r/R\right)^{0.36}\theta^{0.16}} \tag{56}$$

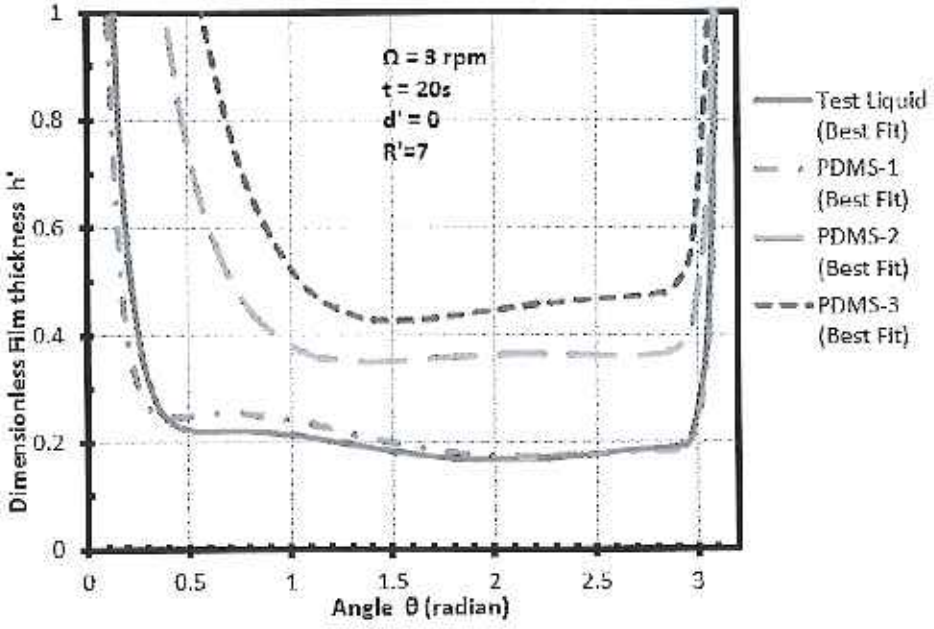

Figure 10. Effect of viscosity on film thickness profiles

Figure 10 shows the predicted film thickness profiles using correlation relationship (56). It can be seen from Figure 10 that the film thickness changes significantly and becomes thicker with the increase of the liquid viscosity. This can be seen from equation (49) since the film thickness is proportional to the viscosity to power 2/3.

4.1. Comparison of the simulations results

The simulations were also compared with the asymptotic solutions of Afanasiev *et al.*[9].

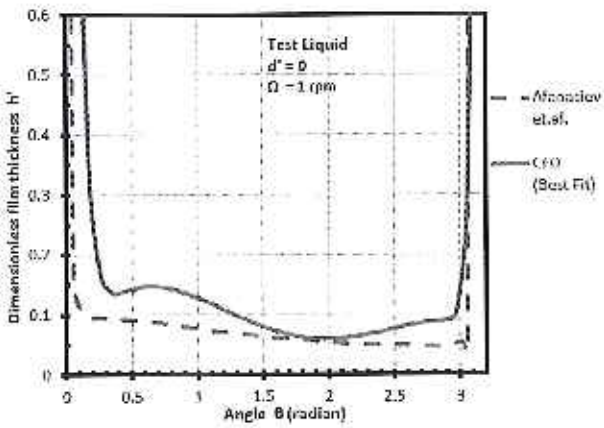

Figure 11a. Film thickness comparison at $\Omega = 1\,rpm$

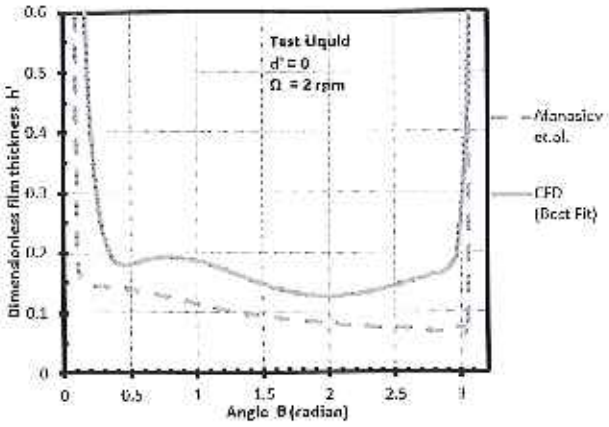

Figure 11b. Film thickness comparison at $\Omega = 2\,rpm$

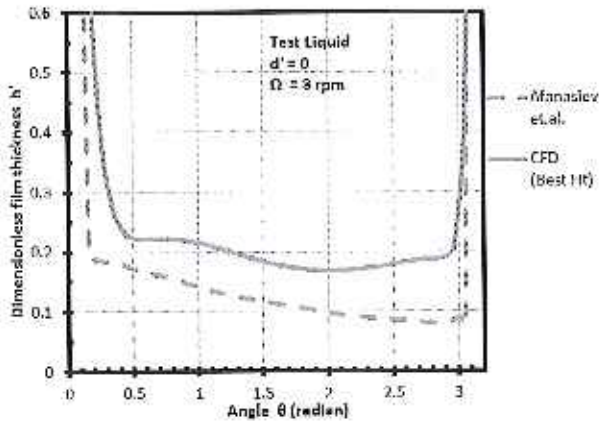

Figure 11c. Film thickness comparison at $\Omega = 3\,rpm$

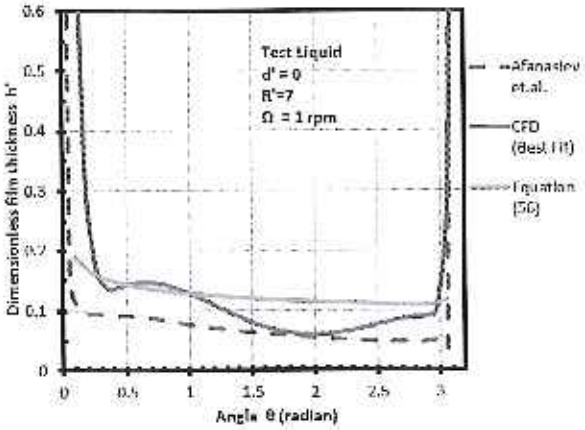

Figure 11d. Comparison of the film thickness profile

The data from Afanasiev *et al.*[9] was extracted graphically and the CFD results are consistent, see Figure 11a-11c. It can be seen from Figure 8a-8c that there is a difference between the film thickness profile in the drag-out and drag-in regions predicted by CFD modelling and that obtained by Afanasiev *et. al.* [9]. A possible reason for this difference is that the Afanasiev *et al.* [9] solution does not fully reflect the influence of the surface tension, but this requires further investigation. The predicted film thickness profile using correlation Equation (56) is a very close approximation, as shown in Figure 11b, to the solutions obtained by Afanasiev *et al.* [9].

4.2 Numerical results for the vertically rotating disc of finite thickness

The thickness of the rotating disc has an influence on the film thickness profile [32, 33]. For the gravitational effect the film formed on the edge of the disc trends to fall over to the surface of the disc and so the thickness of the rotating disc varies as shown in Figure 12.

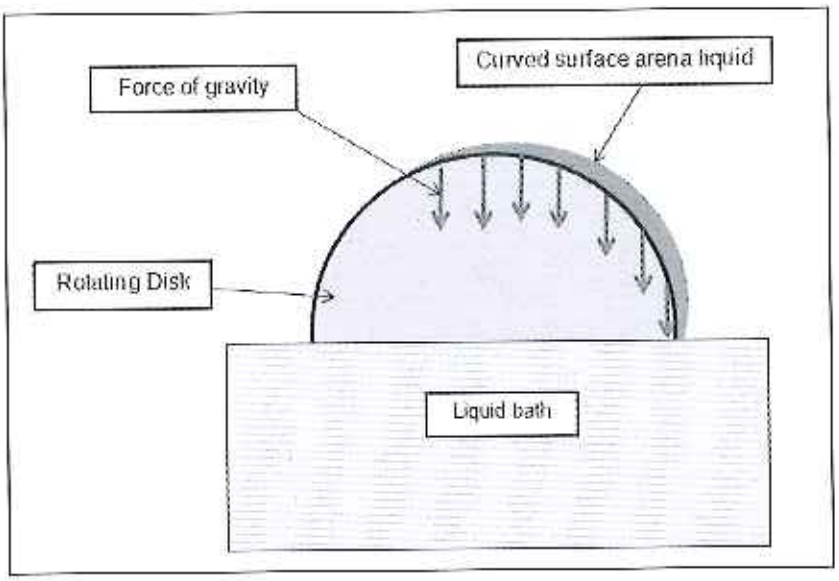

Figure 12. Simplified influence of the gravity influence

The thickness of the rotating disc is denoted by l' and for different values of l' the CFD simulation results are presented in Figure 13. We can see that the film thickness profile varies with the thickness of the disc.

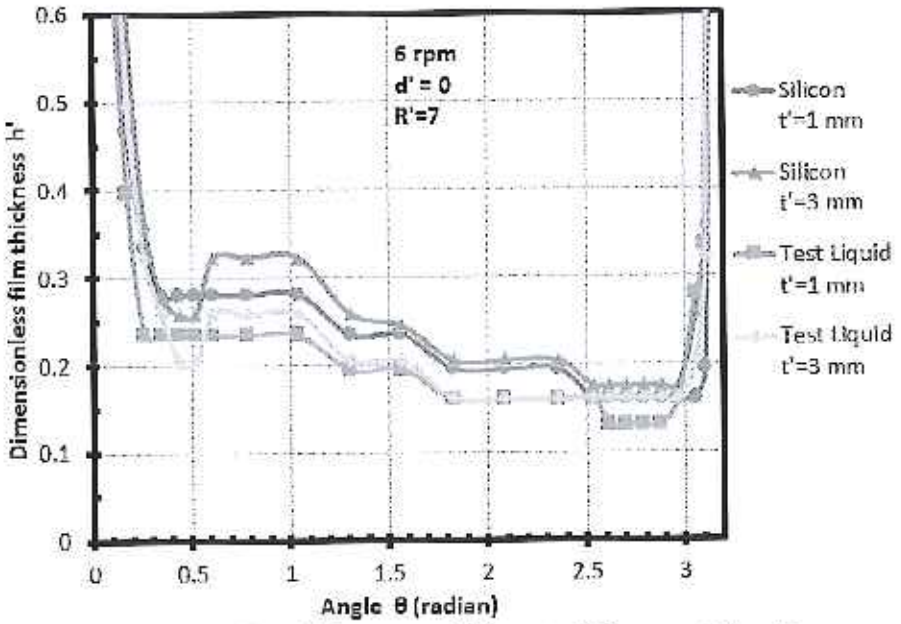

Figure 13. Film thickness at different thickness of the disc

If the thickness of the rotating disc increases from 1mm to 3mm, then there is an increase in the film thickness profile apart from some variations in the drag out and drag in regions.

5. Experimental Investigation

The accurate measurement of film thickness is vitally important and a number of film thickness measurement methods have been developed, and trialled for practical and achievable precision and reliability. Various techniques of film thickness measurement have previously been investigated and described, such as needle contact method, electrical conductance method, capacitance methods, optical method, ultrasonic pulse echo method, and the fluorescence method [34, 35]. Optical techniques are usually preferred for measuring thin film thickness as they are more accurate, non-destructive and require little or no sample preparation. Laser based techniques are described by Oliveira *et.al.* and Wegener and Drallmeier [36, 37].

For conducting the experiments a small laboratory scale experimental device has been designed and manufactured as shown in Figure 14. The dimensions of the rotating disc and the experimental volume have been taken as for those described for the CFD simulations.

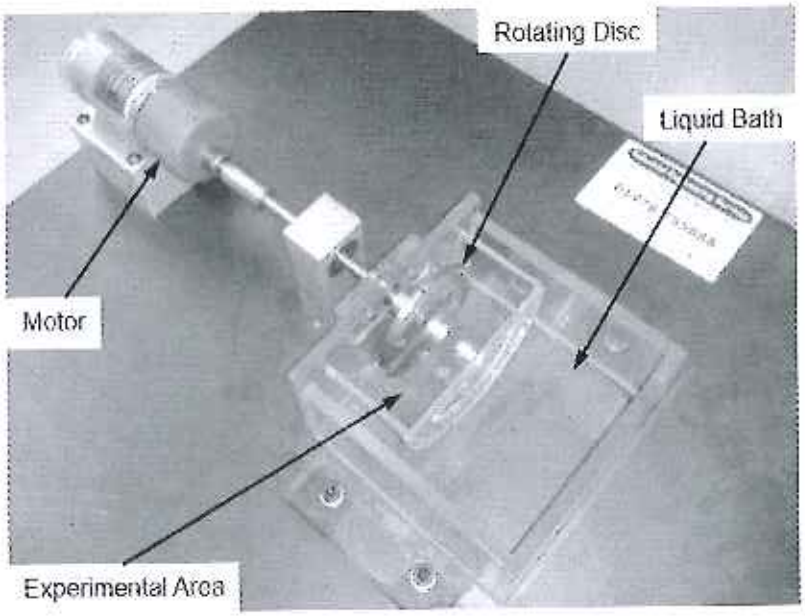

Figure 14. Small laboratory scale experimental device

The experimental volume partially isolated from the liquid bath to avoid the build up of any flow streams towards the disc, which would cause instabilities in film formation. The rotating disc has been designed such way so that it can be replaceable.

Figure 15. Two rotating discs of thickness $t' = 0.5$mm and 3 mm (left and right respectively)

For illustrating the edge effect of the rotating disc on film formation, two different designs of the rotating disc were chosen for the experiments. To obtain a 0.5 mm rim thickness, a disc of 3 mm thickness disc has been chamfered by 2.5 mm x 45^0, as shown in Figure 15. Both the discs have manufactured in stainless steel in order to maintain surfaces smooth enough for stable film formation.

To conduct the experiments the liquids of different viscosities have been used as shown in Table 3.

Table 3. Properties of the liquids used in the experiments

	μ (Pa.s)	σ (N/m)	ρ (kg/m^3)
Silicon liquid	1.48	0.037	985
Scyal solution	1.236	0.050	1032.3
Senegal solution	1.012	0.052	1083

The particular issue of laser light scattering, caused by the white colour of the PDMS-1, was mitigated by mixing the fluid with 5% gum Arabic solution. The new properties of the liquid were achieved as shown in Table 3, named Silicon liquid.

5.1. Laser scan method

In the present study, the laser scan experimental measurements were made using FARO laser scanner. The experimental data was processed in the software package 'Geomagic Qualify 2012'. The FARO laser scanner comprises of two parts, the articulated arm and the scanner attachment at the end as shown in Figure 16.

The articulated arm is a co-ordinate measurement machine, consisting of three dimension encoders at every joint on the arm so that the position of the laser scanner is captured at all times during the scanning. The scanner is attached at the end of the arm, which finds the position of an object by sending out a laser beam that is then reflected back to the sensor on top of the laser emitter. Using both of these parts in unison the scanner can determine the exact position of the points on the

surface of an object from which a digital image can be constructed. The Faro Laser scanner is accurate to ±35μm and can scan at a rate of 19,200 points per second [38].

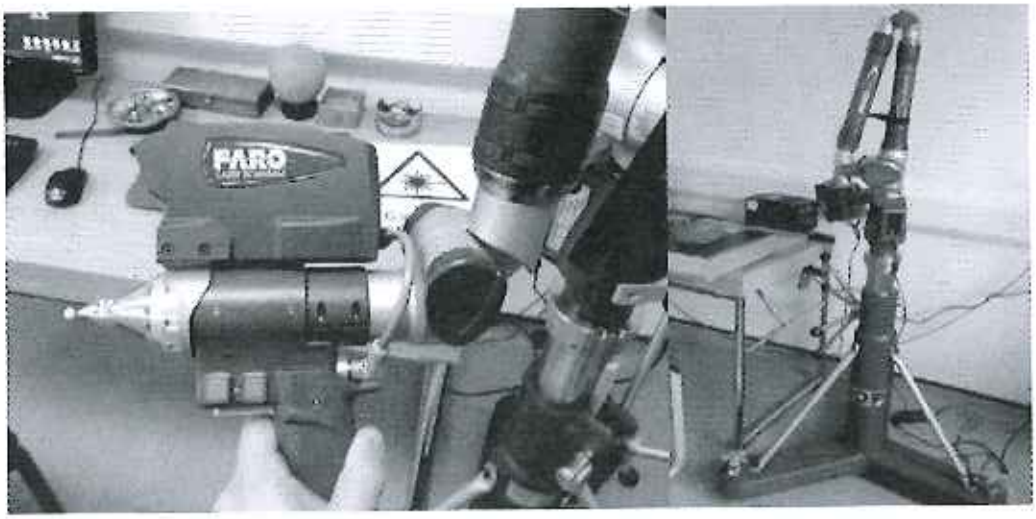

Figure 16. Arrangement for film thickness measurement by laser scan method

A reference image was created of the rotating disc without any liquid film, and subsequent images created after the liquid film formation was stable on the disc surface. The difference between the two images defines the film thickness.

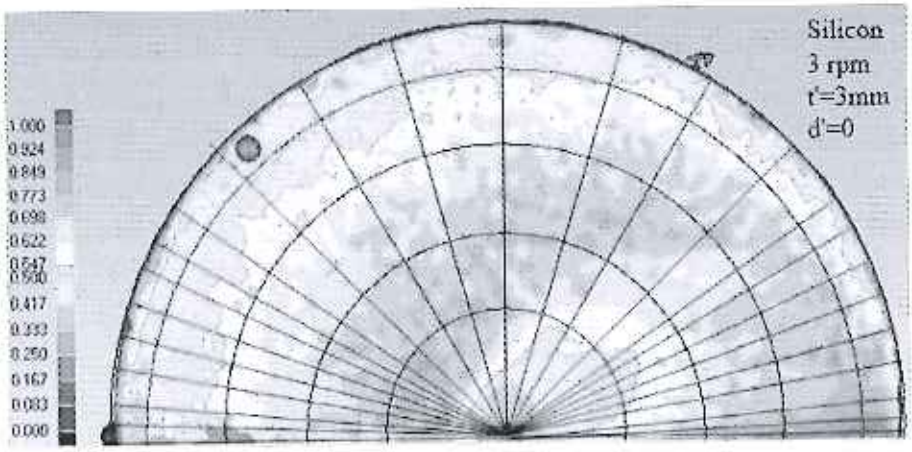

Figure 17. Film thickness distribution on the rotating disc.

A special attribute, the '3d Analysis' feature in the software package Geomagic Qualify 2012, takes a reference plane and compares it to a new plane of the users choice. Once the analysis has

been completed, a colour coded map of the film thickness variation with position is created as shown in Figure 17.

To obtain accurate film thickness data, calibration of the laser scan raw data is necessary. In this study, the calibration was performed mechanically, using a micrometre to measure the liquid film thickness on a level horizontal flat surface and comparing that with measurements obtained using the laser scan method, to obtain a scaling factor. The scaling factor accounts for variation in the experimental set-up and the scattering of the lights during the laser scanning. In this case the scaling factor was found to be of 2.413.

5.2. Experimental results and discussions

It is noticeable from the experiments as shown in Figure 18 that there is no fluid covering the centre of the rotating disc (red circle), and also that the film has a tendancy to move towards the right hand side of the disc (marked in white) under anticlockwise rotation. This is a result of gravitational and capillary effects. The agreement with the CFD simulation result is shown in Figure 7.

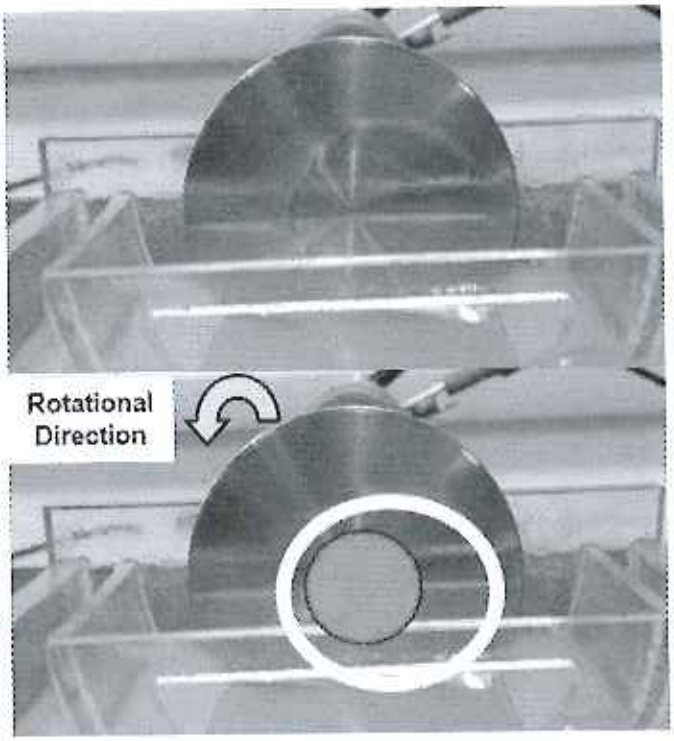

Figure 18. Film formation on the rotating disc.

The experimental results obtained in the present study are consistent with those obtained in the CFD simulations as shown in Figure 19, the shape of the film is generally comparable in form, however the CFD predicted film thickness is slightly higher than found in the experiment. The difference in the average film thickness is 0.0493 mm, and the estimated error is calculated in this case is 7.5%. A possible explanation is numerical diffusion.

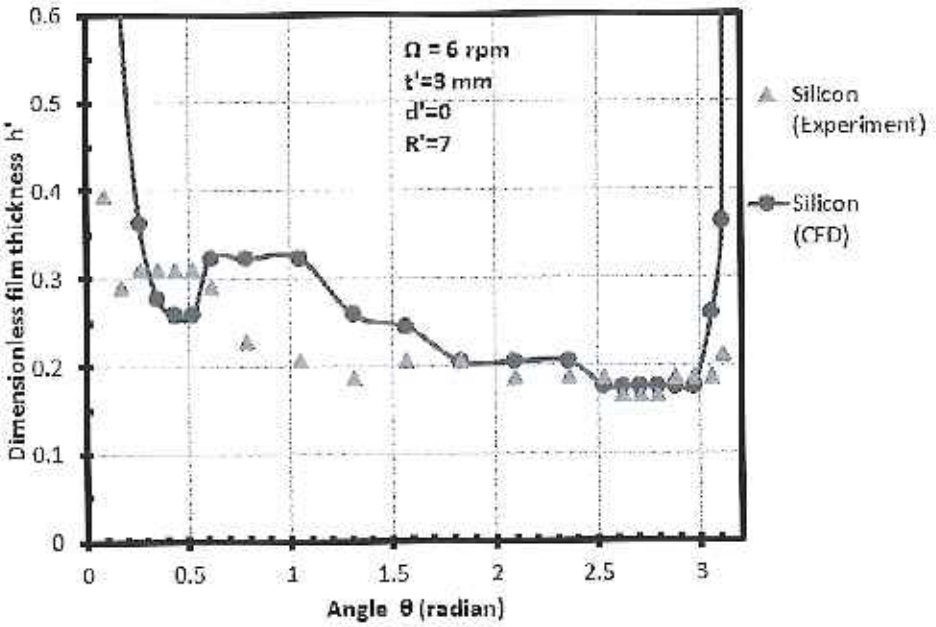

Figure 19. Comparison of the film thickness profile.

From the CFD simulations results the film thickness was estimated by correlation equation (56), simplified form of this equation gives

$$h' \propto \frac{Ca^{0.1} Fr^{0.32}}{\mathrm{Re}^{0.2}} \tag{57}$$

Equation (57) can be further simplified to identify the dominant terms in film formation as

$$h' \propto \frac{\mu^{0.3} \Omega^{0.54}}{\sigma^{0.1} \rho^{0.2} g^{0.32}} \tag{58}$$

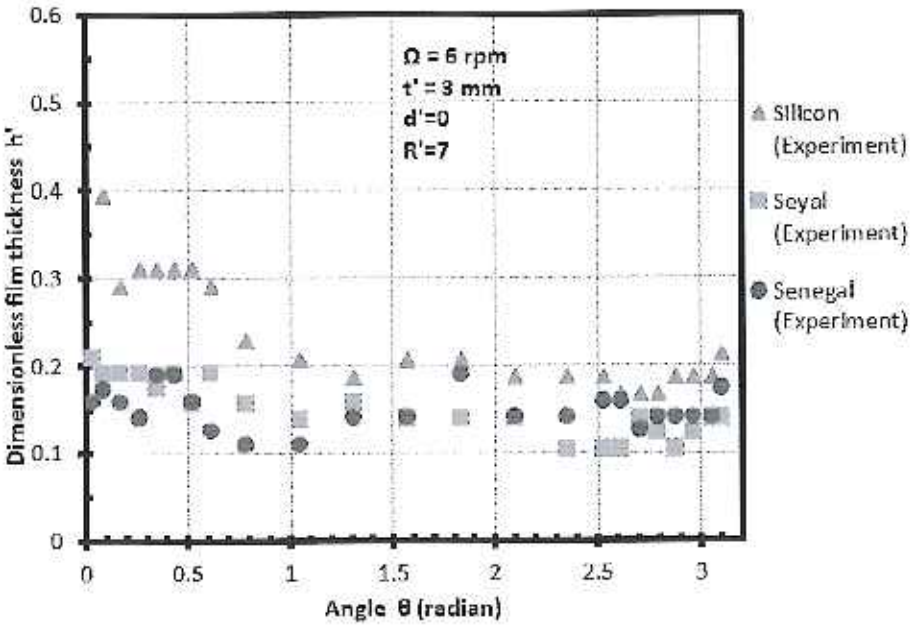

Figure 20. Film thickness profile for liquids of different viscosities.

From equation (58), the two main dominant factors can be identified: viscosity and rotating speed. The experimental results illustrate that there is a significant increase in the film thickness with the increase of the viscosity as shown in Figure 20, which are consistent with the CFD simulation results.

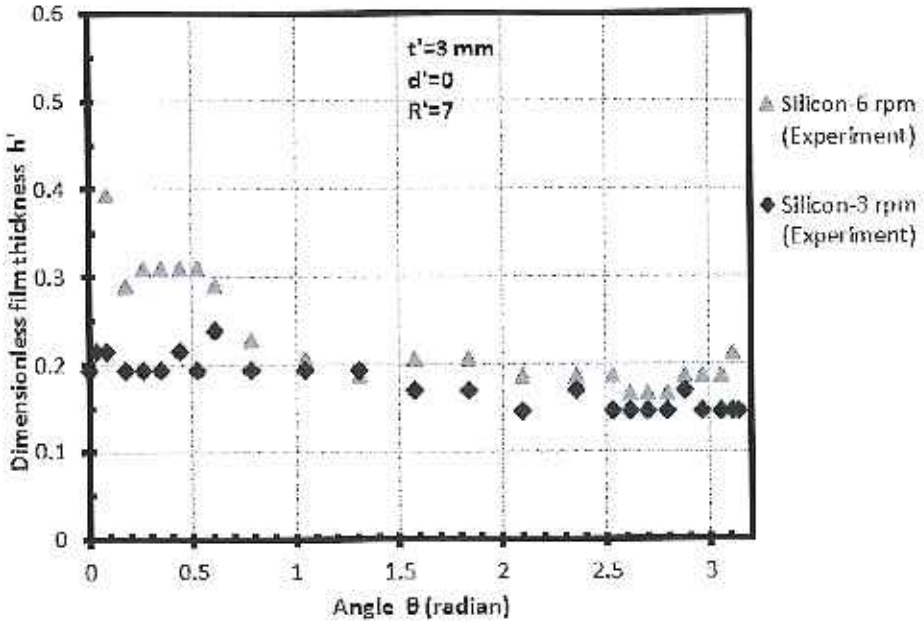

Figure 21. Film thickness profile at different rotating speeds.

The other dominant factor effecting the film thickness in equation (58) is rotating speed. The experimental results are obtained at different rotating speeds as shown in Figure 21, which is a good agreement with those obtained in CFD simulations.

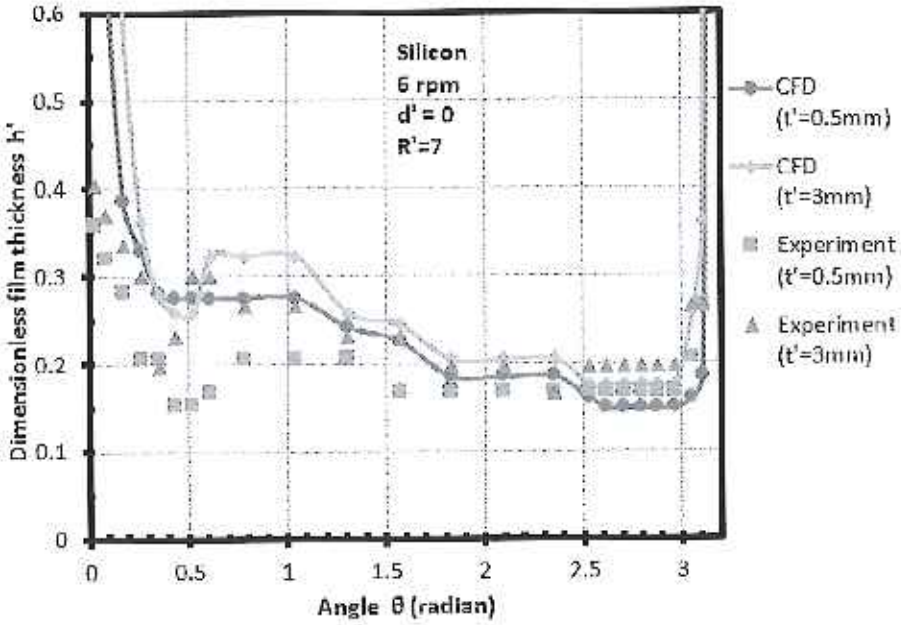

Figure 22. Film thickness distribution on the discs of different thickness.

The rim thickness of the rotating disc affects the film thickness as the film from the rim flows onto the surface of the disc. This gives rise to an increase in the film thickness, as an additional gravitational effect, and this is illustrated in the experimental results, Figure 22, and consistent with the 3D CFD simulation results where the finite rim thickness was modelled.

6. Conclusion

The formation and thickness profile of a thin film on a vertically rotating disc partially immersed in liquid has been modelled numerically to obtain predictions of the thin film thickness distributions. Based on CFD simulation results, a correlation is proposed to describe the film thickness distribution by defining the dominating factors controlling the thin film flows. It was found from the simulations that the two main dominant factors controlling the film thickness profile are the viscosity and rotational angular velocity.

The film thickness increases significantly with increase of the angular velocity of the disc, consistent with the findings as reported in the published literature [9]. The change in the film thickness and the shape of the thin film can be characterized by the Froude number, which is by definition the ratio of the rotating speed and the gravitational force. Since for the case of the vertically rotating disc, the gravitational force is a dominant term, it is to be expected to have a significant influence on the shape of the film. The simulation also confirms that an increase in the viscosity causes the average film thickness to increase, confirming that the Capillary and the Reynolds numbers are significant dimensionless parameters in thin film flow analysis for the viscous effect. The effect of the surface tension on the film thickness profile can be examined by incorporating the Webber number.

An increase in the rim thickness of the rotating disc leads to an increase in the film thickness, as the film formed on the flows downwards onto the surface of the disc. This is a gravity effect, and the CFD simulation results have been illustrated to be consistent with the experimental results.

The experimental results were consistent with those results obtained from the CFD simulations. The average film thickness was over-predicted by about 7.5% by the CFD, and this is thought to be caused by numerical diffusion errors.

Acknowledgements

The authors wish to acknowledge the contributions of Xiaobing Huang and Zoubir Zouaoui to the project.

References

[1] Parmar N. H., Tirumkudulu M. S. and Hinch E. J., (2009) 'Coating flow of viscous Newtonian liquids on a rotating vertical disc', *Physics of Fluids*, **21**, 103-102.

[2] Cheong S. I. & Choi, K. Y., (1995) 'A study on the polymer layer-forming phenomena in a rotating disc polycondensation reactor'. *Journal of Applied Polymer Science,* **55** (13), 1819-1826.

[3] Mouza A. A., Paras S. V., and Karabelas A. J., (2002) 'The influence of small tube diameter on falling film and flooding phenomena', *Int. J. of Multiphase Flow*, **28**, 1311–1331.

[4] Thomas S., Esmaeeli A., and Tryggvason G., (2010) 'Multiscale computations of thin films in multiphase flows', *Int. J. of Multiphase Flow*, **36**, 71–77.

[5] Zhang F., Wu Y. T., Geng J., and Zhang Z. B., (2008) 'An investigation of falling liquid films on a vertical heated/cooled plate', *Int. J. of Multiphase Flow*, **34**, 13–28.

[6] Yu S. H., Lee K. S., and Yook S. J., (2009) 'Film flow around a fast rotating roller', *Int. J. of Heat and Fluid Flow*, **30**, 796–803.

[7] Landau L. and Levich B., (1942) 'Dragging of a liquid by a moving plate', *Acta Physicochim. URSS*, **17**, 42–54.

[8] Wilson S. D. R., (1982) 'The drag-out problem in film coating theory', *J. Eng. Math*, **16**, 209–221.

[9] Afanasiev K., Munch A. and Wagner B., (2008) 'Thin film dynamics on a vertically rotating disc partially immersed in a liquid bath', *App. Math. Modeling*, **32**, 1894–1911.

[10] Sadighi, A., Ganji, D. D. & Sabzemeidani, Y., (2008) 'A decomposition method for volume flux and average velocity of thin film flow of a third grade fluid down an inclined plane'. *Adv, Theor. Appl. Mech.*, **1** (1), 45 - 49.

[11] Idowu, I. A. & Adewuyi, J. B., (2010) 'Relationship between continuity and momentum equation in two dimensional flow'. *African Journal of Mathematics and Computer Science Research*, 3(2), 31-35.

[12] Bird, R. B., Stewart, W. E. & Lightfoot, E. N., (2007) 'Transport Phenomena'. *John Wiley & Sons, Inc.*, **Second Edition**.

[13] Aubin J., Fletcher D. F. and Xuereb C., (2005) 'Design of micro mixers using CFD modelling', *Chem. Eng. Science*, **60**, 2503 – 2516.

[14] Myers T. G. and Charpin J. P. F., (2001) 'The effect of the Coriolis force on axisymmetric rotating thin film flows', *Int. J. of Non-Linear Mechanics*, **36**, 629-635.

[15] Myers T. G. and Lombe M., (2006) 'The importance of the Coriolis force on axisymmetric horizontal rotating thin film flows', *Chem. Engg. and Processing*, **45**, 90–98.

[16] Sung L., Jasmin J., Gu X., Nguyen T. and Martin J. W., (2004) 'Use of laser scanning confocal microscopy for characterizing changes in film thickness and local surface morphology of UV-exposed polymer coatings', *JCT Research*, **1** (4), 267–276.

[17] Fugere J., Gaboury S., Tremblay R. (2012) 'Leibniz rules and integral analogues for fractional derivatives via a new transformation formula', *Bulletin of Math Analysis and Applications*, **4** (2), 72-82.

[18] White, F. M. (2006) 'Viscous Fluid Flow'. *McGraw Hill,* ***Third Edition.***

[19] Lan H., Friedrich M., Armaly B. F. and Drallmeier J. A., (2008) 'Simulation and measurement of 3D shear-driven thin liquid film flow in a duct', *Int. J. of Heat and Fluid Flow*, **29**, 449–459.

[20] Hasan N. and Naser J., (2006) 'Determining the thickness of liquid film in laminar condition on a rotating drum surface using CFD', *Chem. Eng. Science*, **64**, 919 – 924.

[21] FLUENT 6.3 User's Guide (2006), Fluent Inc.

[22] Kim J., (2006) 'Adaptive Mesh Refinement for Thin Film Equations', *Journal of the Korean Physical society'*, **49**(5), 1903 – 1907.

[23] Gao D., Morley N. B. and Dhir V., (2003) 'Numerical simulation of wavy falling film flow using VOF method', *J. of Comp. Physics*, **192**, 624-642.

[24] Haroun Y., Legendre D. and Raynal L., (2010) 'Volume of fluid method for interfacial reactive mass transfer: Application to stable liquid film', *Chem. Eng. Science*, **65**, 2896 – 2909.

[25] Cerne G., Petelin S., and Tiselj I., (2001) 'Coupling of the interface tracking and the two-fluid models for the simulation of incompressible two-phase flow', *Journal of Computational Physics*, **171**(2), 776–804.

[26] Lian, C., Xia, G. & Merkle, C. L., (2009) 'Solution-limited time stepping to enhance reliability in CFD applications', *Journal of Computational Physics,* **228,** 4836 - 4857.

[27] Kheshgi H. S., Kistler S. F. and Scriven L. E., (1992) 'Rising and falling film flows: viewed from a first-order approximation', *Chem. Eng. Science*, **47**(3), 683-694.

[28] Yu S. H., Lee K. S., and Yook S. J., (2009) 'Film flow around a fast rotating roller', *Int. J. of Heat and Fluid Flow*, **30**, 796–803.

[29] Matar O. K. and Lawrence C. J., (2006) 'The effect of surfactant on the flow of a thin liquid film over a spinning disc', *Chem. Eng. Science*, **61**, 1074 – 1091.

[30] Krechetnikove R. and Homsy G. M., (2006) 'Surfactant effects in the Landau–Levich problem', *J. Fluid Mech.*, **559**, 429–450.

[31] Vijayraghvan K. and Gupta J. P., (1982) 'Thickness of the film on a vertically rotating disc partially immersed in Newtonian liquid', *Ind. Eng. Chem. Fundam,* **21**, 333-336.

[32] Zenkour A. M and Mashat D. S, (2010) 'Analytical and Numerical solutions for a rotating annular disc of variable thickness', *Applied Mathematics,* **1**, 431-438.

[33] Campanella O. H and Cerro R. L, (1984) 'Viscous flow on the outside of a horizontal rotating cylinder: The roll coating regime with a single fluid', *Chemical Engineering Science,* **39**, 1443-1449.

[34] Schlom D. G., Chen L. Q., Pan X., Schmehl A., and Zurbuchen M. A., (2008) 'Thin film approach to engineering functionality into oxides', *J. Am. Ceram. Soc.*, **91** (8), 2429 – 2454

[35] Garapon S. G., Heid G., Lavergne G. and Simonin O., (2003) 'Thin wall liquid film thickness measurement: A video optical technique', *Proceedings of PSI/VIP-4,* June 3-5.

[36] Oliveira F. S., Yanagihara J. I and Pacifico A. L., (2006) 'Film thickness and wave velocity measurement using reflected laser intensity', *J. Of the Braz. Soc. Of Mech. Sci. & Eng.*, **28** (1), 30 – 36.

[37] Wegener J. L. and Drallmeier J. A., (2010) 'Measurement of thin liquid film characteristics using laser focus displacement instruments for atomization applications', *ILASS-Americas 22nd Annual Conference on Liquid Atomization and Spray Systems, Cincinnati, OH,* 1 – 14.

[38] FARO, (2012) 'FARO Laser Scan Arm® V3', *04REF201-276-EN - FARO Laser Scan Arm V3 Tech. Sheet.* **1** (2), 1-2.